Femtosecond photomodulation spectroscopy of *a*-Si:H and *a*-Si:Ge:H alloys in the midinfrared

J. A. Moon* and J. Tauc
Department of Physics and Division of Engineering, Brown University, Providence, Rhode Island 02912

J.-K. Lee and E. A. Schiff
Department of Physics, Syracuse University, Syracuse, New York 13244

P. Wickboldt and W. Paul
Division of Applied Sciences, Harvard University, Cambridge, Massachusetts 02138
(Received 10 January 1994; revised manuscript received 20 May 1994)

We present the results of a low-intensity femtosecond pump and probe study of hydrogenated amorphous silicon (*a*-Si:H) and its germanium alloys (*a*-Si:Ge:H) in the probe spectral regions of 0.52–0.81 and 1.19–1.48 eV. We find that the picosecond photoinduced change in the energy and time dependence of the complex dielectric constant is consistent with a model for the injected carrier relaxation which combines extended-to-tail and tail-to-tail thermal carrier transitions, and which uses an optical probe sensitivity to carriers in the localized tail states. The measurements on *a*-Si:H are in quantitative agreement with our model over the entire probe spectral range and from subpicosecond to nanosecond probe delay times; however, we find only qualitative agreement between the model and the pump-probe results of two series of *a*-Si:Ge:H alloys prepared under different conditions. Fits to the subpicosecond data of both the *a*-Si:H and *a*-Si:Ge:H samples indicate that the carriers are initially trapped into the tail states with a characteristic attempt frequency at least eight times higher than the rate at which they are subsequently trapped into deeper tail states.

I. INTRODUCTION

In recent years there has been an intense effort put forth to understand carrier relaxation in hydrogenated amorphous semiconductors. This effort has been spurred both by these materials' interesting physical properties and by their mounting technological applications. Due to efficient optical absorption and low fabrication cost (compared to crystalline silicon), hydrogenated amorphous silicon (*a*-Si:H) and its germanium alloys *a*-Si_x:Ge_{1-x}:H are competing alternatives to crystalline technology for many optoelectronic applications.[1]

In the past decade, advances in ultrashort pulse duration lasers have allowed an examination of carrier dynamics on subpicosecond time scales using optical probe techniques.[2] A variety of techniques such as pump-probe,[3] transient grating,[4] and optical time-of-light (TOF) (Ref. 5) have been used to illuminate subpicosecond carrier dynamics in *a*-Si:H. Searching for highly mobile carriers, Ackley, Tauc, and Paul[6] applied picosecond pump-probe techniques to amorphous silicon. In the next decade, a number of other groups[7–12] undertook similar experiments, and to this day there has been considerable controversy over the interpretation of the experimental results.

To summarize these results, at low intensities (injected carrier densities $n \lesssim 10^{17}$ cm^{-3} per pump pulse) recombination within the multiple trapping model well describes the temporal decays,[3,7] although the mechanism for induced absorption is not agreed upon. As the pump intensity is increased, on subpicosecond times the decays in absorption become faster with a characteristic intensity dependence of the decay time of approximately $n^{-\gamma}$, where $\gamma \sim 0.5-1$, which has been interpreted as due to an Auger-like recombination process.[11] At longer (100 ps to ns) times, the decays are also intensity dependent, and can be fit within a bimolecular recombination picture.[7] At the highest intensities, the photoinduced absorption spectrum probed between 1.2 and 2 eV is proportional to the inverse square of the probe energy and vanishes within a picosecond or so, with a highly damped plasma model in the effective-mass approximation usually invoked as an explanation.[12] In this case the effective subpicosecond decay time of the induced absorption is also intensity dependent, but it is no longer a simple power law of the injected carrier density.[13]

At low injected carrier densities there are major unresolved questions remaining in ultrafast photomodulation spectroscopy measurements on amorphous semiconductors of the last decade. This work attempts to answer some of these questions by overcoming an experimental deficiency: Femtosecond lasers, at the time of these previous measurements, were capable of directly producing only a single-center wavelength (usually 620 nm or 2 eV). This was a serious limitation, since the spectral signature of the probe response is the clearest indication of the physical process involved. In order to generate a "broad" femtosecond probe spectrum (1.3–2.5 eV), a variety of pulse amplification/nonlinear mixing techniques could be used,[14,15] all of which reduce the pulse repetition rate (and hence signal-to-noise ratio) and neces-

sarily increase the pulse intensity, precluding low pump level experiments.

We therefore constructed a femtosecond optical parametric oscillator for this work which allowed the probe pulse energy to be tuned to as little as 0.52 eV, while keeping the pump energy fixed at 2 eV. This advance has allowed a spectrally resolved photomodulation study with ~200-fs time resolution to be undertaken, and the picosecond and subpicosecond dynamics of carriers to be explored more fully than was possible before.

The paper is organized as follows. In Sec. II, the laser system is described, and the methods of data acquisition and analysis are outlined. In Sec. III, the model used to fit the experimental data is described. In Secs. IV and V the main experimental findings are discussed; Sec. IV details the results on *a*-Si:H, and Sec. V contains the results of the experiments on *a*-Si:Ge:H alloys. Finally, in Sec. VI the conclusions are summarized.

II. EXPERIMENTAL TECHNIQUES

A. The femtosecond optical parametric oscillator

At the outset of this study only a single source existed for the generation of synchronized visible and infrared femtosecond pulses at high repetition rates. Edelstein, Wachman, and Tang[16] demonstrated the first cw mode-locked optical parametric oscillator (OPO) based on intracavity pumping a $KiTiOPO_4$ (KTP) crystal in a colliding pulse mode-locked (CPM) ring dye laser. They obtained excellent results in both stability (stable for hours) and tunability of the OPO (~0.35 to 1.7 eV possible for KTP and multiple OPO mirror sets). A drawback to this system lay in the fact that the output coupler of the CPM was replaced by a high reflector in order to increase the intracavity intensity, which rendered the visible (2 eV) output power too small for photomodulation studies. We overcame this limitation by using the "six-mirror" design of Valdmanis and Fork[17] for the CPM cavity, and copying the design of Edlestein for the OPO cavity. The resulting laser system typically gives 15–22-mW average output power at 2 eV at around 250-fs pulse duration, and tunable outputs from the OPO at 0.5–2-mW levels at about 120–250-fs pulse widths typically (depending on alignment). Further details of this laser system can be found in Refs. 18 and 19.

By using two sets of OPO cavity mirrors, a probe energy range of 0.52–0.81 eV in the idler and concurrently 1.48–1.19 eV in the signal could be covered. This range is significantly broader than any used to date in femtosecond amorphous semiconductor photomodulation studies, and approaches the range of tungsten lamps used in microsecond photomodulation studies.[20]

B. Data acquisition

A detailed schematic of the "pump-probe" experiment is shown in Fig. 1. The laser pulses generated by the CPM/OPO enter the experiment on two paths (the pump and probe paths). The pump path contains an acousto-optical modulator which modulates the pulse train at 0.8 or 3 MHz (depending on the type of probe detector used;

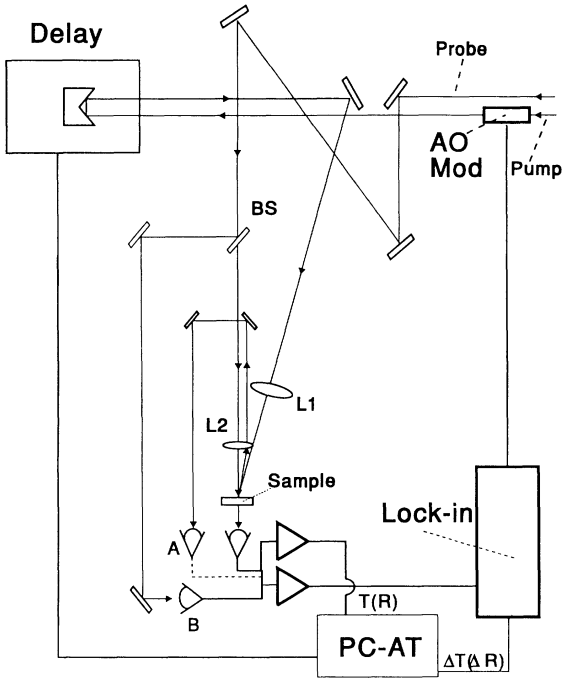

FIG. 1. Detail of experimental apparatus for making pump-probe spectroscopic measurements; $L1=10$-cm focal length; $L2=5$-cm focal length CaF_2; BS, beam splitter; A/B, photodiodes; AO Mod, acousto-optic modulator; PC-AT, personal computer.

see below). The pump pulses are then advanced in time relative to the probe via a stepper-motor-controlled optical delay line. From there the pump pulses are steered into a 10-cm planoconvex-fused silica antireflection coated lens, and onto the sample. The probe line, in order to conserve the low powers coming out of the OPO infrared section, is steered through an uncoated $f=5$ cm CaF_2 lens, which independently focuses the probe on the sample.

The probe light after reflection from or transmission through the sample is then collected on an appropriate photodedector (the "A" detector in Fig. 1). A silicon p-i-n detector was used in the range of 0.6–1.1 μm, and a liquid-nitrogen-cooled InAs detector was used in the range of 1–3.5 μm. The probe signal detected by the photodiode contains both the modulated component (demodulated by a high-frequency lock-in amplifier) and the averaged incident probe power. The output of the lock-in and average incident probe power are digitized and divided in software on an appropriately configured personal computer (which divides out the spectral response of the detection system exactly) for each time delay point yielding either the relative change in refection or transmission ($\Delta R/R$ or $\Delta T/T$). The controlling computer then slews the stage at about one full scan in 30 s (sampled at 300 points for a lock-in output time constant of 10 ms), and stores each scan in memory. A number (usually 10–100) of scans are averaged to improve the signal-to-noise ratio (SNR), the upper limit on total acquisition time being set by the stability of the laser and

the experimentalist's patience. Further details of the detection electronics and techniques may be found in Ref. 19.

C. Data analysis

The pump-probe experiment measures ΔR and ΔT produced by an optical pump pulse. These quantities, unfortunately, usually do not have direct physical meaning. The physics is contained in the time-varying change in the complex dielectric function $\Delta\epsilon(E,t)=\Delta\epsilon_1(E,t)+i\Delta\epsilon_2(E,t)$ produced by the pump and measured by the probe. It is the quantity $\Delta\epsilon$ which enters into Maxwell's equations and can be related to the microscopic processes occurring in the material under study. Because of thin-film interference effects, the change in reflection and transmission combine to give transient decay curves which must be "inverted" by fairly complicated procedures. The errors in calculating $\Delta\epsilon$ from ΔR and ΔT are the main source of uncertainty in studies such as this one; how these uncertainties affect the physical parameters obtained by fitting the $\Delta\epsilon$ data will be mentioned below. We refer the interested reader to Ref. 21 for further details.

III. THEORY

Great progress has been made in recent years in solving the problem of carriers relaxing in the localized states in amorphous semiconductors;[22–27] however, parts of the models lack applicability to the subpicosecond times measured in these experiments. We therefore now outline a more complete model for calculating the change of the dielectric constant $\Delta\epsilon(E,t)$ as a function of probe energy E and time t produced by localized carriers. We must first calculate the distribution of carriers $n(E,t)$ (either electrons or holes) using microscopic transition rates. Once $n(E,t)$ is known, the macroscopic change in $\Delta\epsilon(E,t)$ can be calculated, provided a model for the optical transition mechanism of the probe beam is assumed.

A. Calculation of the injected carrier distribution

The starting point for practically every model of carrier relaxation among localized states is the linearized master equation[22–27]

$$\dot{n}_i=-\sum_{j\neq i}\mathcal{W}_{ij}n_i+\sum_{j\neq i}\mathcal{W}_{ji}n_j-\frac{n_i}{\tau_{ri}}\ , \tag{1}$$

where n_i is the number density of electrons at energy i, $\mathcal{W}_{ij}$ is the transition rate from state i to state j, and τ_{ri} is a monomolecular recombination time which may depend on energy i.

At this point we break Eq. (1) into two parts in energy. One part will deal with the carrier distribution localized in the band tails n_i at energy level E_i. Following Ref. 22, the transition rate between two of these states can be written as

$$W_{ij}=b_{ll}g_l(E_j)dE\begin{cases}\exp\left[\dfrac{-E_{ij}}{k_BT}\right]\ , & E_{ij}>0\\ 1\ , & E_{ij}<0\ ,\end{cases} \tag{2}$$

where b_{ll} is the capture or release cross section (units of $\mathrm{cm}^3\,\mathrm{s}-1$), and where E_{ij} is the energy difference between states i and j, T is the temperature, and k_B is Boltzmann's constant. The density of final states is defined as $g_l(E)$. By defining a constant $\nu_0=b_{ll}g_l(0)dE=b_{ll}N_l(0)$ (units of S^{-1}) this rate can be rewritten as

$$W_{ij}=\nu_0\left[\frac{g_l(E_j)}{g_l(0)}\right]\begin{cases}\exp\left[-\dfrac{E_{ij}}{k_BT}\right]\ , & E_{ij}>0\\ 1\ , & E_{ij}<0\ .\end{cases} \tag{3}$$

We may define a similar rate for transitions between an extended state (above the tail states in energy) and the localized band-tail states as

$$w_{je}=\nu_1\left[\frac{N_e}{N_l(0)}\right]\exp\left[\frac{-E_{ej}}{k_BT}\right]\ , \tag{4a}$$

$$w_{ej}=\nu_1\frac{N_l(E_j)}{N_l(0)}\ , \tag{4b}$$

where w_{je} refers to upward transitions, and w_{ej} refers to downward transitions. We have also defined in analogy to ν_0 a constant $\nu_1=b_{\mathrm{el}}N_l(0)$, where b_{el} is a transition cross section between the extended and localized states, and N_e is the number density of extended states at energy E_e above the mobility edge. The prefactor ν_1 is typically taken to be 10^{12}–10^{13} Hz. For simplicity we assume that like b_{ll}, b_{el} is independent of energy, although some authors have included energy-dependent transition rates in their analyses.[28] As a further simplification, we assume (as in Ref. 22) that the distribution of extended states can be replaced by a single effective extended state at E_e (which we take to be about 25 meV above the mobility edge). With the above specifics in mind, Eq. (1) becomes

$$\dot{n}_i=-\sum_{j\neq i}W_{ij}n_i+\sum_{j\neq i}W_{ji}n_j+w_{ei}n_e-w_{ie}n_i-\frac{n_i}{\tau_r}\ , \tag{5a}$$

$$\dot{n}_e=-\sum_i w_{ei}n_e+\sum_i w_{ie}n_i\ , \tag{5b}$$

where n_e is the number of carriers in the extended state, and we assume that carriers recombine (or alternatively are trapped in deep states) from the tail states with a characteristic time τ_r.

To proceed further, we specify that the density of localized tail states $g_l(E_j)$ for an amorphous semiconductor is exponential in energy below the mobility edge:

$$g_l(E_j)=\frac{\mathcal{N}_l}{k_BT_0}\exp\left[\frac{-E_j}{k_BT_0}\right]\ , \tag{6}$$

where $\mathcal{N}_l$ is the total number of localized states integrated over energy, and k_BT_0 is the characteristic energy width of the tail. We assume that there are approximately the same number of extended states within k_BT of the mobility edge (N_e) as there are localized states ($\mathcal{N}_l$).

The above considerations, with the inclusion of an initial condition, are enough to solve Eq. (5) numerically. We obtain the initial carrier distribution by assuming

that it follows a convolution of the initial and final density of states, and by assuming unit quantum efficiency for the pump photons. The energy is then discretized into $i=1-200$ levels in the tail (with one effective extended level as mentioned above) and Eqs. (5) are evolved in time with a forward differencing scheme, taking care to keep the time step shorter than the fastest inverse transition rate. By finally defining a parameter $\alpha=T/T_0$, i.e., the ratio of the thermal energy to the localized tail energy width, we may completely describe the entire carrier distribution in time and energy with four parameters: α, ν_0, ν_1, and τ_r.

B. Calculation of macroscopic properties

Once the induced carrier distribution is known as a function of energy and time, the change in macroscopic dielectric constant $\Delta\epsilon$ may be calculated. We separate $\Delta\epsilon_2$ into its two parts, "absorption" ($\Delta\epsilon_2^{(a)}$) and "bleaching" ($\Delta\epsilon_2^{(b)}$) (Ref. 29) as

$$\Delta\epsilon_2^{(a)}(\hbar\omega,t)\sim\frac{1}{(\hbar\omega)^2}\left[\int|\mathcal{M}|^2 n(E,t)g_c(E+\hbar\omega)dE + n_e(E_e,t)|\mathcal{M}_E|^2 n_c(E_e+\hbar\omega)\right]+\text{holes} \tag{7}$$

and

$$\Delta\epsilon_2^{(b)}(\hbar\omega,t)\sim-\frac{1}{(\hbar\omega)^2}\int|\mathcal{M}_i|^2 n(E,t)g_v(E+\hbar\omega)dE + \text{holes}\,, \tag{8}$$

where $\hbar\omega$ is the optical probe energy, $|\mathcal{M}|^2(|\mathcal{M}_i|^2)$ is the configuration averaged intraband (interband) matrix element, and $|\mathcal{M}_E|^2$ is the matrix element for optical transitions from the single effective extended state to $\hbar\omega$ higher in the band. Here $n(E,t)$ and $n_e(E_e,t)$ are the electron distributions in the localized and extended states, respectively. g_c (g_v) is the conduction- (valence-) band density of states, and $n_c(E)$ is the number of conduction band states at E in an energy range of k_BT. Since experimentally $\Delta\epsilon_2$ is always observed to be positive, it appears that the values of $|\mathcal{M}|^2$ and $|\mathcal{M}_E|^2$ are much larger than $|\mathcal{M}_i|^2$, so that interband contributions will be neglected. We will therefore identify $\Delta\epsilon_2=\Delta\epsilon_2^{(a)}$.

To obtain the real part of $\Delta\epsilon$, we note that, since the electronic dephasing times are so short,[4] the real part of $\Delta\epsilon$ should adiabatically follow $\mathrm{Im}(\Delta\epsilon)$. We thus calculate $\Delta\epsilon_1(E,t)$ by using the Kramers-Kronig integral transform in E of $\Delta\epsilon_2(E)$.

As an illustration, $\Delta\epsilon$ versus probe energy is calculated in Fig. 2 at two different times. One labeled curve shows the $\Delta\epsilon_2$ response for an $n(E,\nu_0t=1)\sim\exp[E/(k_BT_0)]$ below the mobility edge, and the other labeled curve shows $\Delta\epsilon_2$ calculated from an $n(E,\nu_0t=500)$. Qualitatively, we see that for carriers uniformly spread out over the tail states ($\nu_0t=1$, the initial distribution), an increase of photoinduced absorption as the probe energy decreases is always observed. In the case of an injected carrier distribution peaked around an energy below the mobility edge ($\nu_t=500$), however, there is a peak in $\Delta\epsilon_2$ at a nonzero probe energy. This peak, commonly observed in microsecond photoinduced absorption (PA) studies,[20] moves to higher energy in time due to the carriers thermalizing deeper into the band tails, and arises from the energy gap between the extended final states and the highest occupied level of the localized states.

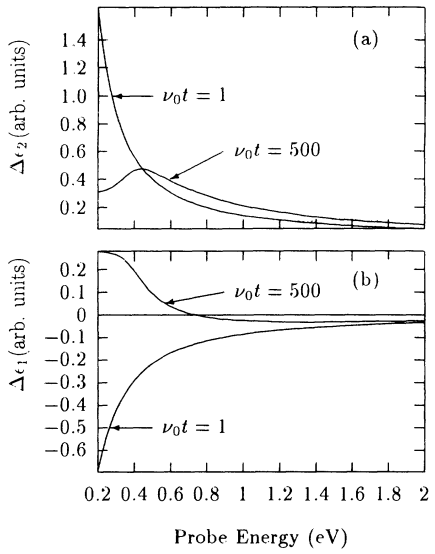

FIG. 2. Change in the imaginary (a) and real (b) parts of the dielectric constants as a function of probe energy at two different times: $\nu_0t=1$ and $\nu_0t=500$. Here $\alpha=0.5$, $\nu_0\tau_r=10^4$, and $E_g=1.7$ eV.

Results for $\Delta\epsilon_1$ calculated from the example $\Delta\epsilon_2$ spectra of Fig. 2(a) are plotted in Fig. 2(b) using the Kramers-Kronig transform. For the first spectrum, at these optical probe energies a negative spectrum for $\Delta\epsilon_1$ is always found. For the case of the second $\Delta\epsilon_2$ spectrum, however, $\Delta\epsilon_1$ is seen to be positive at low probe energies, and then becomes negative only at higher energies.

In Fig. 3 the expected time transients for $\Delta\epsilon$ at three probe energies are shown. There are several features of the decays worthy of note. First, the shapes of the $\Delta\epsilon_2$ decays shown in Fig. 3(a) do not depend on probe energy to a good approximation. An examination of Fig. 3(b), however, shows that the decay rates of the $\Delta\epsilon_1$ curves are energy dependent; at the lowest probe energy the decay shows a significantly faster dependence on time . This result can be understood qualitatively using the Kramers-Kronig relation in the following way. At short times, the bandtails are uniformly occupied, right up to the mobility edge, which leads to increasing $\Delta\epsilon_2$ with decreasing probe energies for all energies. Carriers near the mobility edge are quickly reexcited thermally and trapped into deeper states, leaving a "gap" at longer times between the peak of the carrier distribution and the mobility edge, thus causing the turnover previously shown in Fig. 2. The removal of oscillator strength at low energies contributes strongly to $\Delta\epsilon_1$ even at higher probe energies; the change in absorption at these higher probe energies, however, is

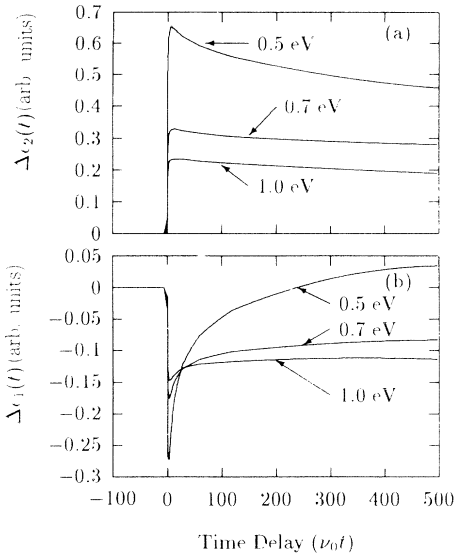

FIG. 3. (a) $\Delta\epsilon_2(t)$ and (b) $\Delta\epsilon_1(t)$ as a function of $\nu_0 t$ for three different indicated probe energies. The same parameters as in Fig. 2 were used.

not significantly affected. We therefore conclude that measurement of the change in the real part of the dielectric constant at low probe energies (e.g., in *a*-Si:H, below 1 eV) is the most sensitive way to probe trapped carriers near the mobility edge on short-time scales.

IV. TIME-RESOLVED PHOTOMODULATION SPECTROSCOPY OF *a*-Si:H

The theoretical and experimental techniques developed in the previous sections will now be applied to thin films of hydrogenated amorphous silicon. This section is broken down into two subsections, for picosecond and femtosecond time scales; in each subsection the main experimental findings are presented first, after which the data are compared to the models developed in Sec. III. All data in this paper are taken at room temperature.

TABLE I. Measured properties of the amorphous semiconductor samples used in this study.

Source	% Ge	d (μm)[a]	E_g (eV)[b]	N_s (cm^{-3})[c]
Syracuse	0	1.58	1.75	4.8×10^{15}
	12	3.52	1.63	3.1×10^{15}
	35	3.55	1.48	3.0×10^{16}
	72	4.11	1.17	2.0×10^{18}
	100	2.25	1.01	6.0×10^{18}
Harvard	17	3.81	1.58	
	48	1.71	1.40	
	70	1.75	1.21	

[a]Film thickness in microns.
[b]Optical gap measured by $(\omega\alpha)^2$ vs ω plot.
[c]Spin density measured from ESR (Ref. 38).

Samples of *a*-Si:H were prepared at Syracuse University in a 13.56-MHz deposition reactor on Corning 7059 glass substrates held at a temperature of 250 °C. A summary of the optical constants for the *a*-Si:H samples used in this section is found in Table I.

A. Picosecond time scales

Figure 4(a) shows the decays of $\Delta\epsilon_2$ in time for *a*-Si:H at two characteristic probe wavelengths. The most "striking" feature to these decays is that they are very similar over at all measured probe energies, being positive at all times (photoinduced absorption, or PA). The decays in the real part of the dielectric constant $\Delta\epsilon_1$ should be compared carefully to those in Fig. 4(a) for $\Delta\epsilon_2$. Figure 4(b) shows that unlike the change in absorption, the change in the real part of the dielectric constant depends on probe energy, and its sign is negative. Qualitatively, the decays become faster as the energy becomes slower.

The negative value of $\Delta\epsilon_1$ already rules out the possibility that band-edge modulation effects dominate the measured signal, since these effects (electroabsorption,[30] thermomodulation,[31] strain[32]) all tend to decrease the gap, thus causing positive contributions to $\Delta\epsilon_1$ at the energies considered. In addition, as we will show below, the photoinduced spectrum of $\Delta\epsilon_2$ at a fixed time delay completely discounts band-edge modulation effects as a major contribution to the measurements.

In this subgap ($E_{\text{probe}} < 1.7$ eV) region, the amplitude of the $\Delta\epsilon_2(E)$ (PA) spectrum is plotted as a function of probe energy at a time delay of 1 ps in Fig. 5. The error bars in the figure are estimated by "inverting" the $\Delta T, \Delta R$ data for different values of the most sensitive parameter λ, the measured laser wavelength. Since fem-

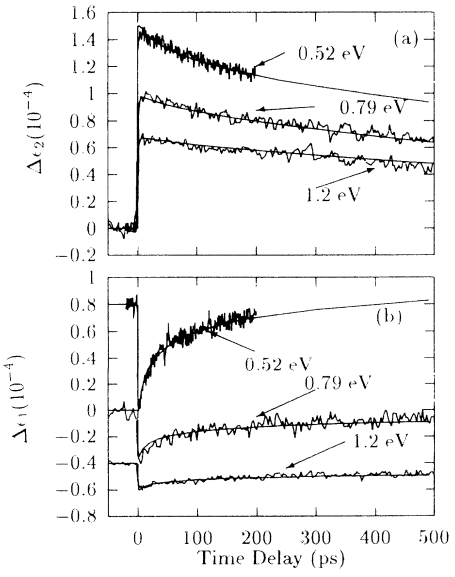

FIG. 4. (a) Transient $\Delta\epsilon_2(t)$ for *a*-Si:H at three different indicated probe energies. (b) $\Delta\epsilon_1(t)$ for *a*-Si:H at three different indicated probe energies. The $\Delta\epsilon_1$ curves are offset for clarity.

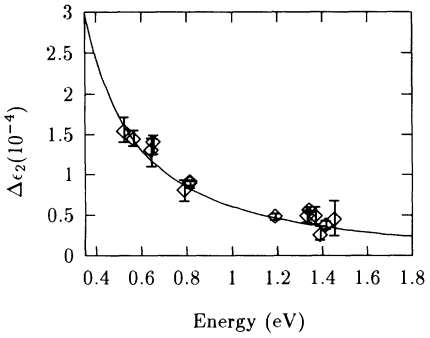

FIG. 5. Measured (points) and fit (line) spectrum of $\Delta\epsilon_2(E)$ for a-Si:H at a fixed time delay of 1 ps.

tosecond pulses have a significant bandwidth $\Delta\lambda(\sim 6-8$ nm at 860 nm in these experiments), the error bars correspond to inverted values for λ, $\lambda+\Delta\lambda/2$, and $\lambda-\Delta\lambda/2$.

Qualitatively the PA spectrum is seen to increase with decreasing probe energy, but only around a factor of 3 between the extremes of the spectrum. This qualitative behavior is similar to that observed on short-time scales by Heppner and Kuhl[10] and Fauchet *et al.*,[12] where the spectrum (measured at much higher pump intensities and over a smaller spectral range) was fit with a Drude model. The spectral response due to heat is qualitatively different than that observed in Fig. 5.

Quantitative fits to any single decay curve measured in this work can be made using the dispersive transport power law[2]

$$\Delta\epsilon_2(t)=\frac{\Delta\epsilon_2(0)}{\left[1+\left[\frac{t}{\tau}\right]^{\alpha}\right]}, \tag{9}$$

where $\alpha=T/T_0$, and τ is related to the recombination time.[22] This law is valid assuming $t\gg\nu_0^{-1}$, but less than the saturation time, and that the experiments are sensitive exclusively to trapped carries in the tails. Using this equation, the decays in $\Delta\epsilon_2$ were fit at a given probe energy using a Levenberg-Marquardt (LM) nonlinear least-squares fitting algorithm.[33] The parameters obtained using this method are listed in Table II. The errors $\delta\alpha,\delta\tau$ listed in Table II are obtained by calculating the final covariance matrix from the fits. Examination of Table II shows that the parameters obtained by fitting the decays in $\Delta\epsilon_2$ at various probe energies are not unique, as would be expected. We therefore must use a more sophisticated model.

In order to fit the complete spectrum of $\Delta\epsilon_1$ and $\Delta\epsilon_2$ simultaneously, a multidimensional LM fitting algorithm was used in conjunction with the model developed in Sec. III. The set of parameters $\{\xi\}$ is chosen to be $\{\xi\}=\{\alpha,\nu_0,\tau_r\}$ defined in Sec. III (the constant ν_1 affects the decays primarily only at shorter times; how ν_1 affects the decays will be discussed in detail below). We assume, following numerous other workers,[2,20,34] that a single type of carrier (i.e., either electrons or holes) dominates

TABLE II. Parameters obtained by fitting each $\Delta\epsilon_2$ transient for a-Si:H individually with a nonlinear least-square fit of three parameters $\{\Delta\epsilon_2(0),\alpha,\tau\}$. The errors $\delta\alpha,\delta\tau$ are obtained by calculating the final covariance matrix from the fit.

Probe energy (eV)	α	$\delta\alpha$	τ (ps)	$\delta\tau$ (ps)	SNR[a]
0.79	0.85	0.04	1157	33	33
1.192	0.87	0.05	1180	41	27
1.37	0.89	0.02	940	39	100
1.40	0.93	0.04	930	47	45

[a]Peak signal-to-noise ratio.

the optical signal, so that only one set of parameters is used. From 2–5 wavelengths each of $\Delta\epsilon_2(t)$ and $\Delta\epsilon_1(t)$ are used in the fits; each transient contains between 300–1000 individual time points, and the individual uncertainty σ is assumed constant for each curve. The uncertainty σ is estimated by individually fitting the individual curves using the LM algorithm with Eq. (9) and calculating the root-mean-square deviation from the fit. Further details of this procedure may be found in Ref. 19.

The temporal shape the $\Delta\epsilon(t)$ transients at different probe energies can be fit excellently within this model, yielding a dispersion parameter $\alpha=0.50$, $\nu_0=4.1$ ps^{-1}, $\tau_r=2.3$ ns, and a reduced overall $\chi^2=1.5$. A more complete listing of fit parameters with estimated uncertainties is given in Table III, and the final fits with data are shown in Fig. 4. Figure 5 shows that the $\Delta\epsilon_2$ spectrum is indeed consistent with the fits, giving further confidence to the model.

It is well established from TOF experiments that $\alpha\simeq 1$ for electrons in a-Si:H at room temperature, i.e,. that the transport is essentially nondispersive [note that we obtain $\alpha=0.93$ at $E_{\text{probe}}=1.4$ eV by fitting Eq. (9) to the decay curve]. It is essential to remember, however, that the optical changes are due to both the contributions of electrons and holes. Since the valence-band-tail energy $k_BT_0\sim 50-60$ meV is significantly larger than the conduction-band-tail (~ 25 meV) energy,[35] a measured value of $\alpha=T/T_0=0.5$ would be consistent with the trapping of holes away from the mobility edge at room temperature. As previously mentioned, it has been postulated that a single carrier type makes the predominant contribution to the change in optical properties, and if

TABLE III. Final full spectral fit parameters obtained for each of the analyzed samples.

Source	% Ge	α	$\delta\alpha$	ν_0 (10^{12} s^{-1})	$\delta\nu_0$ (10^{12} s^{-1})	τ_r (ns)	$\delta\tau_r$ (ps)	χ^2
Syracuse	0	0.50	0.009	4.10	0.007	2.3	150	1.5
	12	0.718	0.001	4.14	0.006	0.47	2	19
	35	0.864	0.002	3.21	0.006	0.46	4	7
	72	0.76	0.006	2.90	0.02	0.32	8	8
Harvard	17	0.92	0.003	5.15	0.04	1.2	16	2.7
	48	1.0	0.003	4.39	0.02	1.65	23	4.1

the dispersive decay power law [Eq. (9)] is used, one would conclude that this carrier type would be electrons. Our method suggests that this may not be the case. In fact, longer time-scale measurements[20,25] also show that the carriers in the valence-band tail dominate the optical signal.

Note that the parameters obtained with the full-spectrum method (Table III) differ significantly from those obtained from the dispersive decay power law (Table II), thus pointing out the need to fit the complete complex change in dielectric constant $\Delta\epsilon(E,t)$ to obtain meaningful results. We again emphasize that fitting the decays in $\Delta\epsilon_2(t)$ at a single wavelength with three or more parameters[3,7,8] can give misleading results due to the nonuniqueness of the chosen parameter set.

Finally, we note that although the uncertainties cited in Table III are small for each fit parameter, a slightly different set of parameters may be obtained by using different optical constants in the "inversion" procedure[21] used to calculate $\Delta\epsilon$ from ΔR and ΔT. In fact, we previously reported different parameters ($\alpha=0.67$, $\nu_0=1.2$ ps^{-1}, and $\tau_r=2.3$ ns) (Ref. 36) when we fit a subset of the $\Delta\epsilon$ data for our a-Si:H samples. In order to make the model fit the full $\Delta\epsilon$ data, we had to recalculate the $\Delta\epsilon$ transients using different (but still within measurement uncertainty) thin-film optical constants. This procedure changes none of our conclusions, but does point out that the uncertainties of the final fit parameters are quite a bit larger than would be indicated from Table III.

B. Femtosecond time scales

The decay of $\Delta\epsilon_2$ at a probe energy of 1.19 eV on a subpicosecond time scale is shown in Fig. 6. The lack of any observable change on time scales less than a picosecond at probe energies above the gap has been verified many times on a-Si:H[3]. Also, recent picosecond TOF experiments[5] have failed to find any electrons in high mobility extended states on time scales shorter than a picosecond, although the signal-to-noise ratio in this experiment was poor. This study verifies that these facts remain true when probed with optical energies significantly below the gap.

It is interesting to note that the model of Sec. III can be used to give correct results on short time scales, as shown in Fig. 6 using two different methods. First, a probe sensitivity to carriers above the mobility edge may be assumed. Unfortunately, the value needed for the ratio of the tail-to-extended matrix element $|\mathcal{M}|^2$ to the extended-to-extended matrix element $|\mathcal{M}_E|^2$ defined as $r_M=|\mathcal{M}_E|^2/|\mathcal{M}|^2$ is not unity (as would be expected if the nature of the electronic states changed little above and below the mobility edge). The agreement using $r_M=0.7$ shown in Fig. 6 may thus be coincidental. An alternative method to fit the data which also gives acceptable results is choosing a trapping rate ν_1 from extended-to-tail states significantly faster than ν_0, the rate of intratail-state trapping. Figure 6 shows that a value of $\nu_1=8\nu_0$ also gives an acceptable fit. Choosing between these alternatives will be deferred to Sec. V.

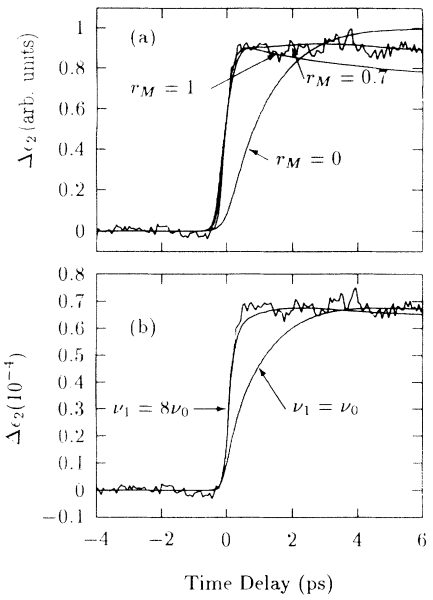

FIG. 6. Transient $\Delta\epsilon_2(t)$ for a-Si:H at subpicosecond times for a probe energy $E_{\text{probe}}=1.19$ eV. (a) The smooth lines are fits using the indicated ratio r_M of optical matrix elements. (b) The smooth curve is a fit using an extended-tail attempt frequency of $\nu_1=8\nu_0$; the curve $\nu_1=\nu_0$ is shown for reference.

V. TIME-RESOLVED PHOTOMODULATION SPECTROSCOPY OF a-Si:Ge:H ALLOYS

The initial time for carriers in extended states to become trapped in localized bandtail states was unresolvable in Sec. V even with the subpicosecond resolution of the OPO system. In an ideal situation the excess energy of the initially injected carriers could be made larger to increase the time required to trap. This method has been used with some success by Wraback and Tauc,[3] who found fast transients in a-Si:H using a pump photon energy of 4 eV. The OPO system did not produce enough intensity to frequency double the pump, so that the only viable way to increase the excess initial carrier energy above the mobility edge is to decrease the optical gap. This can be accomplished by alloying a-Si:H with germanium.

Amorphous silicon-germanium alloys were prepared for this study at Syracuse University and at Harvard University. In the former case, the samples were deposited in a 13.56-MHz deposition reactor on Corning 7059 glass substrates held at 250 °C. Further characterization of these samples can be found in Ref. 38. The samples fabricated at Harvard were deposited in a parallel-plate diode rf reactor by the glow discharge deposition technique using an unpowered electrode. Since the Harvard samples were made under conditions specifically optimized for a-Si:Ge:H alloys (unlike the Syracuse samples, which were made under conditions optimized for a-Si:H), the electronic properties of the two sets of samples may be expected to differ. Complete details of the fabrication process of the Harvard samples can be found in Ref. 39.

The measured properties of the complete set of samples used in this study are summarized in Table I. Seven different alloy concentrations were used in this study, with the Ge content ranging between 12 and 100%. Notice that the optical gap is a linear function of Ge content, going smoothly in energy between *a*-Si:H and *a*-Ge:H. Also, for these thicknesses, all samples were practically opaque at 2 eV (except the unalloyed *a*-Si:H film).

A. Picosecond time scales

As an example of the typical decays and photoinduced spectra obtained from the alloy samples, the results obtained from the 17% Ge alloy made at Harvard are shown in Figs. 7 and 8. Figure 7(a) shows the decays in $\Delta\epsilon_2$ at four probe energies. As in the case in unalloyed *a*-Si:H, the decay rates are quite similar at different probe energies; however, the decay rate is faster than that of *a*-Si:H, a fact which will be fully discussed below. Figure 7(b) shows two decays in $\Delta\epsilon_1$. Again, the qualitative feature of increasing decay rate with lower probe energies is observed, as in *a*-Si:H. The interpretation remains the same as in the unalloyed case, i.e., the decay in $\Delta\epsilon_1$ at low probe energies measures carriers thermalizing away from states near the mobility edge. Finally, the spectrum of $\Delta\epsilon_2$ is plotted at a 1-ps delay for two alloys (17% and 48% Ge) in Fig. 8. As in the unalloyed case, the spectrum of PA increases toward decreasing probe energy. Thermal effects are therefore once again ruled out as the source of these decays, as is any band-edge modulation effect.

Since we see the same qualitative spectral and temporal features in the alloy samples as in *a*-Si:H, we might expect that the model of Sec. III would give a similar excellent fit to the data. The parameters $\{\alpha, \nu_0, \tau_r\}$ obtained in this way are listed in Table III. In fitting the data to obtain these parameters, we again assume that one type of carrier dominates the optical signal. From the reduced χ^2 values in Table III, it is clear that the model gives a

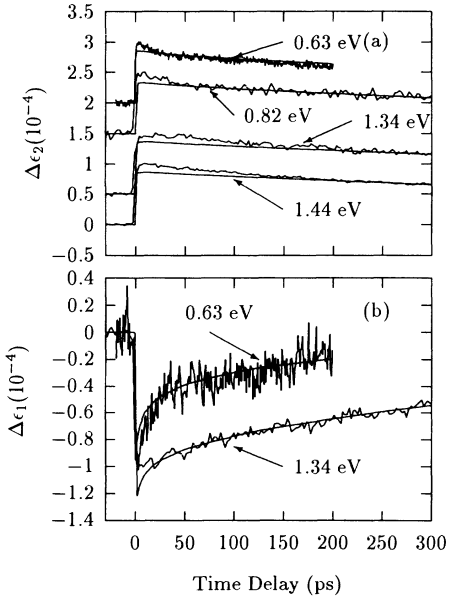

FIG. 7. (a) Change in imaginary index $[\Delta\epsilon_2(t)]$ for a 17% Ge alloy at four different indicated probe energies. (b) Decay of $\Delta\epsilon_1(t)$ at two probe energies. The smooth lines are fits from the model, with the parameters given in Table III. Curves are offset for clarity.

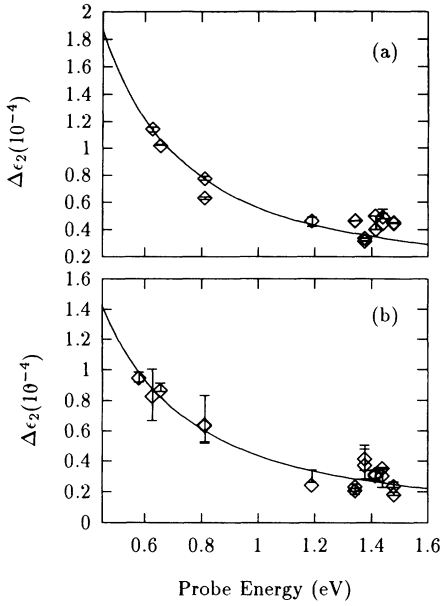

FIG. 8. Example spectra of $\Delta\epsilon_2$ at 1-ps delay for the (a) 17% Ge alloy and (b) 48% alloy prepared at Harvard.

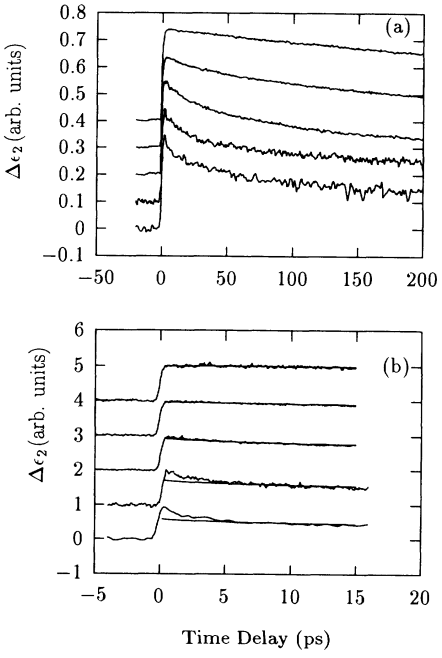

FIG. 9. Dependence of $\Delta\epsilon_2$ decays on alloy concentration at a probe energy of 1.19 eV of the Syracuse series. From slowest to fastest decay: %Ge=0, 12, 35, 72, and 100. Curves are normalized to the same peak value and offset for clarity. (b) Same, but subpicosecond times. The smooth fit curves are obtained by extrapolating the longer (> 200 ps) fits back to zero time delay.

TABLE IV. Empirical parameters obtained from fitting individual $\Delta\epsilon_2(t)$ transients for a given alloy concentration.

Source	% Ge	E_{probe} (eV)	α	$\delta\alpha$	τ (ps)	$\delta\tau$ (ps)	SNR[a]
Syracuse	0	1.19	0.89	0.06	1180	41	27
	12	1.19	0.87	0.02	323	6	59
	35	1.19	0.64	0.01	114	8	56
	72	1.19	0.55	0.04	100	20	25
	100	1.19	0.59	0.03	97	8	24
Harvard	17	1.44	0.877	0.014	528	6.3	71
	48	1.44	0.874	0.016	644	10	67
	70	1.34	0.70	0.021	187	12	37

[a]Peak signal-to-noise ratio.

relatively poor fit to the *a*-Si:Ge:H spectra, even though the qualitative features are similar. The fits can probably be improved if the effect of both types of carriers (electrons and holes) is taken into account in the model, since the rate of carrier thermalization is expected to be different for the different types of carriers. Including this effect in the present model, however, would add three more adjustable parameters, which introduces too much ambiguity into the analysis in our opinion, and thus was not attempted. The best way to separate out the signatures of the different types of carriers will be to measure the temperature dependence of the photoinduced optical signal. This is left for future research.

The systematic increase in decay rate with increasing Ge content may be quantified somewhat further. Figure 9 shows that the decays of $\Delta\epsilon_2$ at a probe energy of 1.19 eV for different alloy concentrations became faster with increasing Ge content. By fitting Eq. (9) to the individual $\Delta\epsilon_2$ decays (the results of which are summarized in Table IV), we see that the decay times at a given Ge concentration for the Harvard series are longer than the Syracuse series. This observation is consistent with the expected electronic superiority of the samples fabricated at Harvard, i.e., that the Harvard samples have a lower defect density than the samples fabricated with the same Ge content by the methods used at Syracuse. This result also illustrates that the decay time τ of Eq. (9) remains a good relative parameter to compare between samples.

The decay time, however, is not proportional to the electron-spin-resonance (ESR)-active dangling-bond defect density, as a comparison of Tables I and IV shows, although this time does decrease with increasing spin density. Even though using a typical $\tau \sim 500$ ps, and a recombination center density of 10^{17} cm^{-3}, a cross section of around 2×10^{-15} cm^2 is obtained, which is typical of neutral recombination centers in solids,[40] we must be somewhat careful in overinterpreting the phenomenological decay time τ. Besides the nonuniqueness problem pointed out in Sec. IV, the repetition rate of the laser is large, so the population trapped in deep states does not go to zero between pulses (i.e., in 10 ns), which complicates the interpretation. Quantitative correlation between the measured spin density and decay rate is thus not possible.

B. Femtosecond time scales

The fits of the longer time data for $\Delta\epsilon_2$ at probe energies near the mobility edge are extrapolated back to time $t=0^+$ in Fig. 9(b), and plotted with the corresponding short-time $\Delta\epsilon_2$ data, showing a departure from the predicted behavior of the asymptotic model on a subpicosecond time scale. In fact, Fig. 9(b) shows that there is a systematically larger "spike" at short times for increasing Ge concentration (i.e., larger initial average energy above the mobility edge).

Since the optical probe energy where the fast transient is largest is above the optical gap energy in the *a*-Ge:H and *a*-Si_{28}:Ge_{72}:H samples, band-edge modulation effects play an important role in these data. The issue can be resolved if instead we use an optical probe energy far below the gap energy. The result of this subgap probe measurement is shown in Fig. 10 for the 100% Ge sample at probe energy of 0.64 eV. The fast transient in $\Delta\epsilon_2$ vanishes [Fig. 10(a)], while $\Delta\epsilon_1$ [Fig. 10(b)] is negative and shows a fast response which is not fully time resolved by the laser system.

We conclude that the fast transient in $\Delta\epsilon_2$ at probe energies near and above the optical gap is due to some sort of band-gap modulation effect. This is not surprising when the data of Thomsen *et al.*[32] are examined, where a large optoacoustic response was found in amorphous Ge for a probe energy of 2 eV(significantly above the band gap). The reason that this is not observed in *a*-Si:H and low concentration alloys is because the optical-absorption length of the pump pulse is up to 150 times longer, giving an insignificant local temperature rise and no appreciable strain in the *z* direction. The remaining fast transient in $\Delta\epsilon_1$, however, because of its negative sign, is due to free-carrier trapping (the sign of $\Delta\epsilon_1$ due to strain is positive deep in the gap). Note that since a fast transient is not observed in the induced absorption of subgap probe energies, the probe is at least no more sensitive to carriers in the extended states than to trapped carriers.

In order to tell whether or not this step response in the induced absorption is due to carriers becoming trapped in the tail states within the time resolution of the experiment or to an optical sensitivity to carriers above the mobility edge, the data were fit using the model of Sec. III. The results are shown in Fig. 10. Either assumption gives acceptable results for the induced absorption, but the results for $\Delta\epsilon_1$ are best fit by assuming that the carriers are trapped very quickly and that the probe is not sensitive to carriers above the mobility edge. Physically this arises because a probe sensitivity to carriers in the extended states give a large oscillator strength at very low probe energies. The shape of the induced absorption at these (unmeasurably, at least in this study) low energies will thus cause a large, negative, quickly decaying response in $\Delta\epsilon_1$ at these relatively higher energies. This is a serious problem with our model in that Eq. (7) is really only valid for optical probe frequencies much higher than the trapping rates ν_0 and ν_1, and thus contributions to $\Delta\epsilon_1$ from $\Delta\epsilon_2$ at these energies may be spurious. It may be possible to remove this discrepancy with a more accurate model for the induced absorption at these low

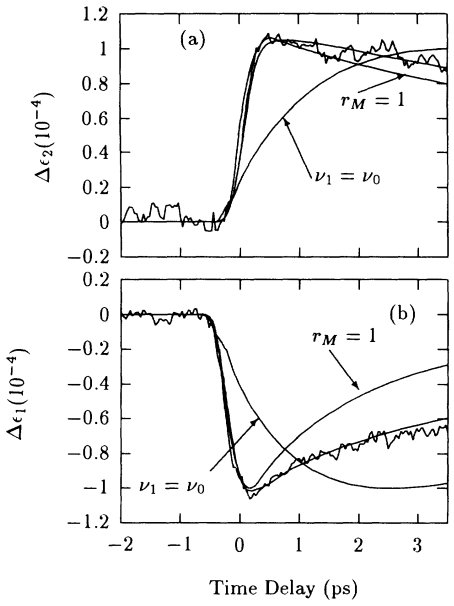

FIG. 10. Subpicosecond $\Delta\epsilon_2(t)$ (a) and $\Delta\epsilon_1(t)$ (b) data for the 100% Ge sample probed far beneath ($E_{\text{probe}}=0.64$ eV) the mobility edge. The smooth fits are obtained using an extended-to-tail transition rate prefactor of $\nu_1=8\nu_0$. The labeled curves are made using $\nu_1=\nu_0$ and $r_M=1$.

probe energies, but this was not attempted.

By using the extended-to-tail transition rate prefactor ν_1 in the model of Sec. III, we obtain $\nu_1 \geq 8\nu_0$; this would give an average carrier energy relaxation rate on the order of or greater than 12 eV ps^{-1} assuming that the carriers have about 0.3 eV to dissipate in $\nu_0^{-1} \simeq 0.025$ ps. This rate is at least a factor of 5 over that which has been previously reported, measured by other means.[13,37]

This result leaves a question: what physical mechanism could underlie such a fast inelastic scattering process in an amorphous solid? A definitive answer is not forthcoming because so little is known for certain about the nature of the extended electronic states. Any calculation of the transition rates will depend sensitively on *ad hoc* assumptions about the wave functions of the carriers. Although mechanisms have been postulated in the literature,[13,37] and more fundamental theoretical approaches have been attempted,[24] the final answer is still not known.

VI. CONCLUSIONS

A low-intensity photomodulation study of amorphous semiconductor thin films has been performed on a femtosecond time scale with a probe energy range comparable to the range covered in the steady state and in microsecond transient studies. This work can be viewed as a set of measurements which has extended by conventional photoinduced absorption studies more than six orders of magnitude in time. By having time resolution on the order of the fundamental carrier trapping rate, the validity of currently accepted models has been critically tested and for the most part vindicated.

The results in this work show that the most sensitive way to probe the initial carrier trapping events in amorphous semiconductor thin films is by examining the real part of the change in the dielectric constant at probe energies significantly below the gap energy. This is due to the indirect nature of the change $\Delta\epsilon_1$: changes in absorption at very low probe energies (meV levels) affect $\Delta\epsilon_1$ at much higher probe energies in a measurable way.

In order to quantify our experimental data, we extended carrier relaxation models to include two different thermal transition rates, one for intratail transitions and one for transitions between the extended states and the tail. The model has all the correct qualitative features of the experimental data, and in unalloyed *a*-Si:H samples the theory is adequate to explain quantitatively the observed behavior. This model also shows from our subpicosecond data that the carriers are trapped out of the extended states extremely quickly, at least eight times faster than they are trapped more deeply between localized tail states. However, we did not attempt to calculate this rate from first principles due to gaps in our knowledge of the underlying material properties. More sophisticated methods of measuring and calculating carrier transport near the mobility edge are thus needed before the physical picture of carrier relaxation in amorphous semiconductors is complete.

ACKNOWLEDGMENTS

We are indebted to Dr. D. C. Edelstein of IBM Yorktown Heights, and Professor C. L. Tang's group at Cornell University for many useful discussions concerning the parametric oscillator used in this work. T. R. Krist is acknowledged for technical assistance. One of the authors (J.A.M.) thanks the IBM Corporation for support. This work was supported by NSF Grant No. DMR 90-14977.

*Present address: Laser Physics Branch, Code 5640, U.S. Naval Research Laboratory, Washington, D.C. 20375.

[1] *Amorphous and Microcrystalline Semiconductor Devices: Optoelectronic Devices*, edited by J. Kanicki (Artech House, Boston, 1991).

[2] J. Tauc and Z. Vardeny, *Critical Reviews in Solid State and Materials Sciences* (Commercial Rubber, Boca Raton, 1990), Vol. 16, p. 403.

[3] Z. Vardeny and J. Tauc, Phys. Rev. Lett. **46**, 1227 (1981).

[4] G. Noll and E. O. Göbel, J. Non-Cryst. Solids **97-98**, 141 (1987); E. O. Göbel and P. Thomas, *ibid.* **141**, 35 (1992).

[5] R. I. Devlen and E. A. Schiff, J. Non-Cryst. Solids **141**, 106 (1992).

[6] D. E. Ackley, J. Tauc, and W. Paul, Phys. Rev. Lett. **43**, 415 (1979).

[7] W. B. Jackson, C. Doland, and C. C. Tsai, Phys. Rev. B **34**, 3023 (1986).

[8] T. L. Gustafsen, H. Scher, D. M. Roberts, and R. W. Collins,

Phys. Rev. Lett. **60**, 148 (1988).
[9]R. I. Devlen, G. S. Kanner, Z. Vardeny, and J. Tauc, Solid State Commun. **78**, 665 (1991).
[10]J. Heppner and J. Kuhl, in *18th International Conference on the Physics of Semiconductors,* edited by D. Engstrom (World Scientific, Singapore, 1986), p. 1033.
[11]A. Esser, K. Seibert, H. Kurz, G. N. Parsons, C. Wang, B. N. Davidson, G. Lucovsky, and R. J. Nemanich, J. Non-Cryst. Solids **114**, 573 (1989); Phys. Rev. B **41**, 2879 (1990); A. Esser, H. Heesel, H. Kurz, C. Wang, M. J. Williams, and G. Lucovsky, J. Non-Cryst. Solids **137-138**, 535 (1991).
[12]P. M. Fauchet, D. Hulin, A. Mingus, A. Antonetti, J. Kolodzey, and S. Wagner, Phys. Rev. Lett. **57**, 2438 (1986).
[13]P. M. Fauchet, D. Hulin, R. Vanderhagen, A. Mourchid, and W. L. Nighan, J. Non-Cryst. Solids **141**, 76 (1992).
[14]*The Supercontinuum Laser Source,* edited by R. R. Alfano (Springer-Verlag, New York, 1989).
[15]D. S. Moore and S. C. Schmidt, Opt. Lett. **12**, 480 (1987); T. M. Jedju and L. Rothberg, Appl. Opt. **27**, 615 (1988); I. Ledoux, J. Badan, J. Zyss, A. Migus, D. Hulin, J. Etchepare, G. Grillon, and A. Antonetti, J. Opt. Soc. Am. B **4**, 987 (1987); J. H. Glwoina, J. Misewich, and P. P. Sorokin, Opt. Lett. **12**, 19 (1987).
[16]D. C. Edelstein, E. S. Wachman, and C. L. Tang, Appl. Phys. Lett. **54**, 1728 (1989); E. S. Wachman, D. C. Edelstein, and C. L. Tang, Opt. Lett. **15**, 136 (1990); E. S. Wachman, W. S. Pelough, and C. L. Tang, J. Appl. Phys. **70**, 1893 (1991).
[17]J. A. Valdmanis and R. L. Fork, IEEE J. Quantum Electron. **QE-22**, 112 (1986).
[18]J. A. Moon, IEEE J. Quantum Electron. **QE-29**, 265 (1993).
[19]J. A. Moon, Ph.D. Thesis, Brown University, 1992.
[20]H. A. Stoddart, Z. Vardeny, and J. Tauc, Phys. Rev. B **38**, 1362 (1988).
[21]J. A. Moon and J. Tauc, J. Appl. Phys. **73**, 4571 (1993).
[22]J. Orenstein, M. A. Kastner, and V. Vaninov, Philos. Mag. B **46**, 23 (1982).
[23]M. Grünewald, B. Movaghar, and D. Würtz, Phys. Rev. B **32**, 8191 (1985).
[24]H. Overhold and P. Thomas, *Electronic Transport in Hydrogenated Amorphous Silicon,* Springer Tracts in Modern Physics Vol. 114 (Springer, Berlin, 1989).
[25]F. W. Schmidlin, Phys. Rev. B **16**, 2362 (1977).
[26]J. Noolandi, Phys. Rev. B **16**, 4466 (1977).
[27]R. Schumacher, Ph.D. Thesis, Phillips-Universität, Marburg, 1991.
[28]D. Monroe, Phys. Rev. Lett. **54**, 146 (1985).
[29]J. Tauc and Z. Vardeny, Philos. Mag. B **52**, 313 (1985).
[30]G. Weiser, U. Dersch, and P. Thomas, Philos. Mag. B **57**, 721 (1988).
[31]M. H. Brodsky and P. A. Leary, J. Non-Cryst. Solids **35+36**, 487 (1980).
[32]C. Thompsen, H. T. Grahn, H. J. Maris, and J. Tauc, Phys. Rev. B **34**, 4129 (1986).
[33]W. H. Press, B. P. Flannery, S. A. Teukolsky, and W. T. Vetterling, *Numerical Recipes in C* (Cambridge University Press, Cambridge, 1988), p. 258 and references therein.
[34]P. R. Wake and N. M. Amer, Phys. Rev. B **27**, 2599 (1983).
[35]W. B. Jackson, S. M. Kelso, C. C. Tsai, J. W. Allen, and S.-J. Oh, Phys. Rev. B **31**, 5194 (1985).
[36]J. A. Moon and J. Tauc, J. Non-Cryst. Solids **164-166**, 885 (1993).
[37]M. Wraback and J. Tauc, Phys. Rev. Lett. **69**, 3682 (1992).
[38]L. Chen, J. Tauc, J.-K. Lee, and E. A. Schiff, Phys. Rev. B **43**, 11 694 (1991).
[39]W. Paul, S. J. Jones, W. A. Turner, and P. Wickbolt, J. Non-Cryst. Solids **141**, 271 (1992).
[40]C. H. Henry and D. V. Lang, Phys. Rev. B **15**, 989 (1977).